LANGMUIR

pubs.acs.org/Langmuir Article

Pb^{2+}-Selective Nanoemulsion-Integrated Single-Entity Electrochemistry for Ultrasensitive Sensing of Blood Lead

Hiranya Madawala, Surendra Raj Puri, Delaney Weaver, and Jiyeon Kim*

Cite This: *Langmuir* 2024, 40, 3004−3014 Read Online

ACCESS | Metrics & More | Article Recommendations | Supporting Information

ABSTRACT: Unequivocally, Pb^{2+} as a harmful substance damaging children's brain and nerve systems, thereby causing behavior and learning disabilities, should be detected much lower than the elevated blood lead for children, 240 nM, endorsed by US CDC considering the unknown neurotoxic effects, yet the ultralow detection limit up to sub-ppb level remains a challenge due to the intrinsically insufficient sensitivity in the current analytical techniques. Here, we present nanoemulsion (NE)-integrated single-entity electrochemistry (NI-SEE) toward ultrasensitive sensing of blood lead using Pb-ion-selective ionophores inside a NE, i.e., Pb^{2+}-selective NE. Through the high thermodynamic selectivity between Pb^{2+} and Pb−ionophore IV, and the extremely large partition coefficient for the Pb^{2+}−Pb−ionophore complex inside NEs, we modulate the selectivity and sensitivity of NI-SEE for Pb^{2+} sensing up to an unprecedentedly low detection limit, 20 ppt in aqueous solutions, and lower limit of quantitation, 40 ppb in blood serums. This observation is supported by molecular dynamics simulations, which clearly corroborate intermolecular interactions, e.g., H-bonding and π^*−n, between the aromatic rings of Pb−ionophore and lone pair electrons of oxygen in dioctyl sebacate (DOS), plasticizers of NEs, subsequently enhancing the current intensity in NI-SEE. Moreover, the highly sensitive sensing of Pb^{2+} is enabled by the appropriate suppression of hydroxyl radical formation during NI-SEE under a cathodic potential applied to a Pt electrode. Overall, the experimentally demonstrated NI-SEE approach and the results position our new sensing technology as potential sensors for practical environmental and biomedical applications as well as a platform to interrogate the stoichiometry of target ion−ionophore recognition inside a NE as nanoreactors.

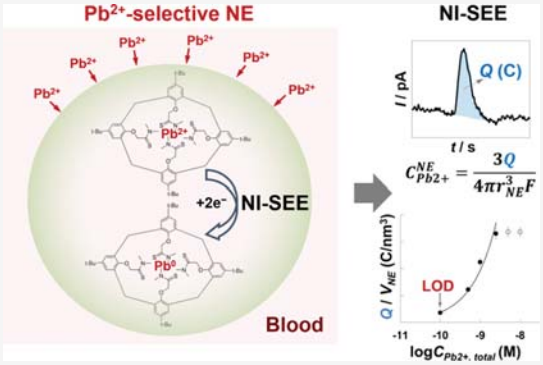

INTRODUCTION

Sensing toxic small molecules at an ultralow limit of detection (LOD) is of great importance, as their exposure under out-of-control conditions, even at a very low concentration, may lead to extensive perils to human health. Especially, the urgent need for the ultrasensitive detection of blood lead is broadly significant, since lead exposure to human is responsible for 143,000 annual deaths and 0.6% of the global burden of disease.[1−3] Childhood lead exposure under the age of 5 is particularly risky, since lead can adversely affect and slow down the development of body, brain, and metabolism.[4] In fact, lead exposure in childhood causes annually c.a. 600,000 of new cases for children with intellectual disabilities, thereby leading to behavior and learning disabilities, hearing problems, headaches, and delayed growth.[4] Emotional and anxiety problems can significantly rise even at a small increase in the blood lead level.[5] Accordingly, the evaluation of elevated blood lead (EBL) and the efforts to reduce children's lead exposure have been a long-standing concern for public health. Recently, the Centers for Disease Control and Prevention (CDC) has lowered the definition of EBL from 60 to 5 μg/dL (i.e., 50 ppb),[6,7] close to the LOD of 3.3 μg/dL of the clinically utilized sensor, LeadCare II, whereas no safe level of lead has been defined. A lower EBL, however, is anticipated, as no threshold of blood lead has been established considering the neurotoxic effect.[8]

Traditional approaches for blood lead sensing include electrochemical methods, e.g., anodic stripping voltammetry (ASV),[1] atomic absorption spectroscopy (AAS),[9] and inductively coupled plasma mass spectrometry (ICP-MS).[10] Despite the remarkable LODs of ICP-MS (0.5−2 ppb)[11,12] and graphite furnace AAS (10 ppb),[13] small sample size, and reasonable analysis time, the high cost of instrumentation and running as well as the high level of operator's skill limits their broad access and applicability. LeadCare II based on ASV has been commercially available at low cost and utilized to perform blood lead measurements in the range of 3.3−65 μg/dL at a point of care with a rapid analysis time in less than 5 min.[1] It,

Received: October 16, 2023
Revised: January 17, 2024
Accepted: January 17, 2024
Published: January 31, 2024

https://doi.org/10.1021/acs.langmuir.3c03138
Langmuir 2024, 40, 3004−3014

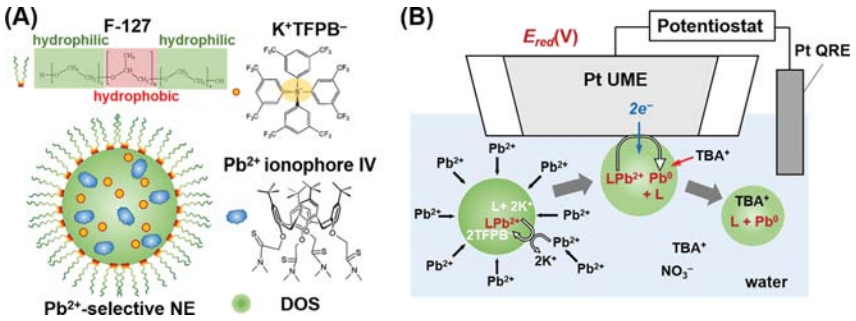

Figure 1. (A) Schematic illustrations of major components, surfactants (Pluronic F-127), cation exchanger (KTFPB), Pb^{2+} ionophore IV, and dioctyl sebacate oil (DOS) for a Pb^{2+}-selective NE and the hypothesized structure of a NE. (B) Scheme of SEE measurements using Pb^{2+}-selective NEs to selectively separate/preconcentrate Pb^{2+} from water (or aqueous sample solutions) to NEs with an exchange of K^+ and electrochemically sense preconcentrated Pb^{2+} by reduction (E_{red} = −0.4 V vs Pt QRE) upon the collision of a NE onto a Pt UME.

however, is barely sensitive to detecting even lower EBL, thus being limited for future applications. Another electrochemical approach is potentiometric-ion-selective electrodes (ISEs) utilizing a plasticized polymer membrane doped with ionophore.[14,15] The analyte ion−ionophore complexation in the membrane develops an equilibrium phase boundary potential across the membrane/sample solution interface showing the logarithmic dependence on analyte ion activity or concentration. Highly sensitive ISEs with nano-picomolar Pb^{2+} LOD have been developed for drinking water, while limitations have remained in response time and direct measurements in blood.[16,17] Seriously, slow and concentration-dependent response time varying 2−50 min was exhibited due to the slow and concentration-dependent ion-exchange process at the macroscopic interface of membrane/water.[18] Unpredictable concentration of the unknown sample disables the concentration-dependent adjustment of the response time. Furthermore, the given membrane-sandwiched system cannot reach true equilibrium, thus challenging the accuracy and precision in measurements.

Recently, we have explored nanoemulsion (NE)-integrated single-entity electrochemistry (NI-SEE) as sensors for ultratrace level analysis with sub ppb level of LOD as a result of high sensitivity and fast response under true equilibrium owing to the unprecedentedly high preconcentration factor and effective mass transport, respectively.[19,20] The rapid mass transport of analytes to NEs enabled fast and true equilibrium in the NE system due to the small size of NEs, thereby leading to high accuracy and precision as well as in situ real-time SEE measurements.[19] SEE is a modern electrochemical technique, where a change in current or potential is measured upon an individual collision of nanosized features onto a micro- or nanosized electrode.[21] Broadly, SEE has been employed for polydisperse nano−micro emulsions or nanoparticles to discretely study variations in their size or electrocatalytic activities, respectively.[21] Contrarily, we introduced highly monodisperse NEs to SEE and opened up unique applications of SEE to explore the fundamental understanding of the NE system such as the NE interfacial structure[22] and the in situ determination of a partition coefficient at individual intact NEs.[20] Moreover, analytical processes using the SEE and monodisperse NEs could be innovatively advanced with high sensitivity, rapidity, miniaturization, and easy accessibility with reasonable costs as well as high precision and accuracy.[19]

Further, the modularity of the NE system by incorporating chemical functionalities offers the ability to decorate the selectivity of NEs, governing molecular-level interactions between the target analytes and a NE, affording selective sensing toward certain analytes. Deliberately, it is straightforward to design and synthesize NEs for discerning the recognition of leads in blood through interactions between Pb^{2+} and Pb^{2+}-selective ionophores. Hence, we investigated intriguing ion-selective NEs by combining SEE that offers a highly discriminative sensing behavior for lead with an ultralow LOD. The rugged NE system can afford direct measurements of blood samples with negligible biofouling as well. Here, we successfully demonstrated Pb^{2+}-selective NI-SEE for blood lead sensing and quantification, where the ultralow LOD and lower limit of quantitation (LOQ) could be achieved at 20 ppt level in aqueous sample solutions and at sub-ppb level in the blood serums, respectively. We synthesized highly monodisperse Pb^{2+}-selective NEs by incorporating thioamide derivative with the calixarene group of ionophore, i.e., *tert*-butylcalix[4]arene-tetrakis(*N*,*N*-dimethylthioacetamide) (a.k.a., Pb^{2+} ionophore IV), exhibiting both high affinity toward lead(II) cations ($\log \beta_n > 15.0$)[23] and high selectivity with no major interfering ions ($\log K^{pot}_{Pb^{2+},M^{n+}} < -3.0$)[24] (Figure 1A). The resulting NEs are used as Pb^{2+}-selective nanoextractors and combined with SEE to effectively separate, extract Pb^{2+} from aqueous sample solution, preconcentrate it to NEs, and detect Pb^{2+} in situ via electrochemical reduction (Figure 1B). For sensitive and reproducible analysis, the fundamental design of a sensing system needs to be optimized: (1) In SEE measurements, electrochemical reduction of Pb^{2+} in a NE should be efficiently facilitated inside a NE, (2) the hydroxyl radical formation under a cathodic potential applied to a Pt ultramicroelectrode (UME) should be suppressed because hydroxyl radicals deteriorate/rupture NEs, induce a leakage of Pb^{2+} from NEs, and subsequently disable Pb^{2+} sensing during SEE, (3) a large partition coefficient of Pb^{2+}−Pb^{2+} ionophore IV at an intact NE is required to accommodate an extremely high preconcentration of Pb^{2+} in a NE, thus enabling a high sensitivity in SEE. Under the optimized system, ultrasensitive Pb^{2+} detection with Pb^{2+}-selective NI-SEE could be achieved in aqueous sample solutions containing Pb^{2+} ranging from 100 pM to 10 μM in the presence of various concentrations of NEs at 80 fM−8 pM. We constructed a calibration curve by plotting charge densities at single NEs determined from a series of SEE measured in standard aqueous sample solutions versus total Pb^{2+} concentrations and validated the analytical utility of Pb^{2+}-selective NI-SEE by accurately determining Pb^{2+} in blood serums throughout spiked blood sample tests. Markedly, the application of Pb^{2+}-selective NEs

https://doi.org/10.1021/acs.langmuir.3c03138
Langmuir 2024, 40, 3004−3014

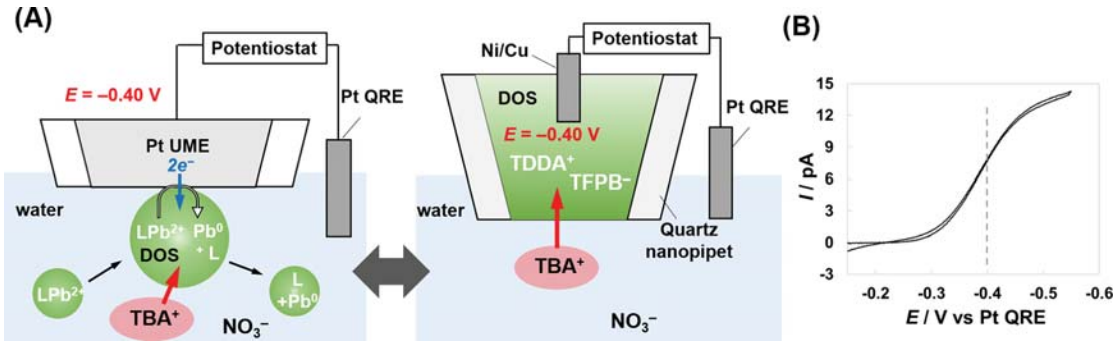

Figure 2. (A) Schematic illustration of (left) the electron transfer reaction (i.e., Pb^{2+} reduction) coupled with ion transfer reactions (i.e., TBA^+ ingress) in NE during the SEE; (right) DOS-filled nanopipet-supported ITIES mimicking a NE for the nanopipet voltammetry of TBA^+ ion transfer reaction. (B) Nanopipet voltammograms of TBA^+ ion transfer in the presence of 1 mM $TBANO_3$ in the aqueous solution. The scan rate is at 25 mV/s.

and SEE exhibited unprecedentedly low LOD at a few 10 ppt in aqueous samples and also successful utilization in direct blood measurements with sub-ppb level of Pb^{2+} with a negligible matrix effect.

RESULTS AND DISCUSSION

Fundamental Design of Pb^{2+}-Selective Electrochemical Sensing. *Ion Transfer-Facilitated Electrochemical Reduction of Pb^{2+} Inside NEs.* Strongly hydrophilic Pb^{2+} cannot be transported across the NE interface either spontaneously or even in the affordable potential window. It is the complex formation between the Pb^{2+}-selective ionophore and Pb^{2+} that makes Pb^{2+} transfer across the NE interface possible. Accordingly, Pb^{2+}-selective NEs are introduced to extract and partition Pb^{2+} from aqueous solutions into NEs for electrochemical sensing.

The partitioning of Pb^{2+} into a NE additionally requires an ion exchange with a cation, e.g., K^+ from a KTFPB cation exchanger existing in a NE for electroneutrality (Figure 1B). K^+ ion transfer from a NE to aqueous phase should be thermodynamically favorable since K^+ is highly hydrophilic. The resulting Pb^{2+} partitioned in a NE can be electrochemically sensed by its reduction upon the collision of a NE onto a Pt UME under a cathodic potential (Figure 1B). To fully and steadily accommodate the electrochemical reduction of Pb^{2+} in a NE until their complete electrolysis, appropriate ion-transfer reaction should be coupled with the reduction of Pb^{2+} inside a NE, which can maintain the electroneutrality in a NE.[22] Specifically, the steady reduction of Pb^{2+} to Pb^0 consumes positive charges in a NE, thus demanding additional cations transferred from the aqueous phase to a NE for electroneutrality. Hence, $TBA^+{\cdot}NO_3^-$ is selected for not only supporting electrolytes in the aqueous bulk solution but also coupled ion transfer to facilitate the electron transfer reaction of Pb^{2+} reduction. Importantly, facile TBA^+ ion transfer should be considered to exclude the possibility that a coupled ion transfer is the limiting factor in the overall electrochemical sensing.

Herein, we utilized a nanopipet-supported interface between two immiscible electrolyte solutions (ITIES), and we experimentally proved that TBA^+ ion transfer across the NE interface is more facile than the electrochemical reduction of Pb^{2+}. A nanopipet was filled with supporting electrolytes ($TDDA^+TFPB^-$) and DOS solvent, same as the plasticizers of NEs, and immersed in the aqueous solution containing $TBANO_3$, thereby mimicking the NE interface (Figure 2A). Under the given conditions, the organic phase in the nanopipet represents the body of NEs, where the ingress of cations, TBA^+ from aqueous bulk solution across ITIES, was studied by nanopipet voltammetry with sweeping potential toward the negative direction. The resulting voltammograms of 1 mM TBA^+ are shown in Figure 2B. Since TBA^+ is a fairly hydrophobic cation, the voltammogram of TBA^+ ion transfer appears at less negative potentials with $E_{1/2}$ = −0.38 V versus Pt QRE, implying a facile ion transfer from aqueous to the organic phase.[25] Accordingly, more than half of the diffusion-controlled currents is acquired for TBA^+ ion transfer at −0.4 V versus Pt QRE, where the electrochemical sensing of Pb^{2+} reduction is conducted (see the Supporting Information (SI) and Figure S1). −0.4 V versus Pt QRE is nearly close to the onset potential for Pb^{2+} electrochemical reduction in the organic solution, e.g., inside a NE, thereby kinetically controlling Pb^{2+} reduction, whereas facile TBA^+ ion transfer is achieved across the NE interface. Strategically, we chose −0.4 V versus Pt QRE, a less negative potential for Pb^{2+} sensing, to suppress the extensive formation of hydroxyl radicals during SEE measurements. More details about radical formation and its suppression are discussed in the next section. Overall, electrochemical reduction of Pb^{2+} inside a NE is not limited by the interfacial ion transfer of TBA^+ but facilitated while retaining the electroneutrality in a NE during SEE measurements.

Scavenging $OH^{\cdot}$ Radicals for the Sensitive Detection of Pb^{2+} in Intact NEs. At a cathodic potential, −0.4 V or more negative versus Pt QRE, Pb^{2+} partitioned to NEs undergoes electrochemical reduction upon the collision of a NE onto a Pt UME, while O_2 in the aqueous solution can be reduced at a Pt UME as well in the aerobic condition. In this given condition, we could not observe any distinctive current spikes caused by the reduction of Pb^{2+} inside NEs during SEE measurements. We suspect that the oxygen reduction reaction (ORR) at the Pt surface leads to the concurrent production of reactive oxygen species (ROS) such as hydroxyl ($HO^{\cdot}$) radicals.[26] This reactive radical attacks most of the organic molecules nonselectively due to the high oxidizing power.[26] In fact, $HO^{\cdot}$ radical production is thermodynamically plausible at the reduction potential of O_2 at neutral pH (E° = +0.39 V vs NHE at pH 7)[27] as below

$$O_2 + 2H^+ + 3e^- \rightarrow HO^{\cdot} + OH^- \quad (1)$$

$HO^{\cdot}$ is able to react with the organic solvent via H abstraction or addition of hydrocarbons, thereby leading to secondary

https://doi.org/10.1021/acs.langmuir.3c03138
Langmuir 2024, 40, 3004−3014

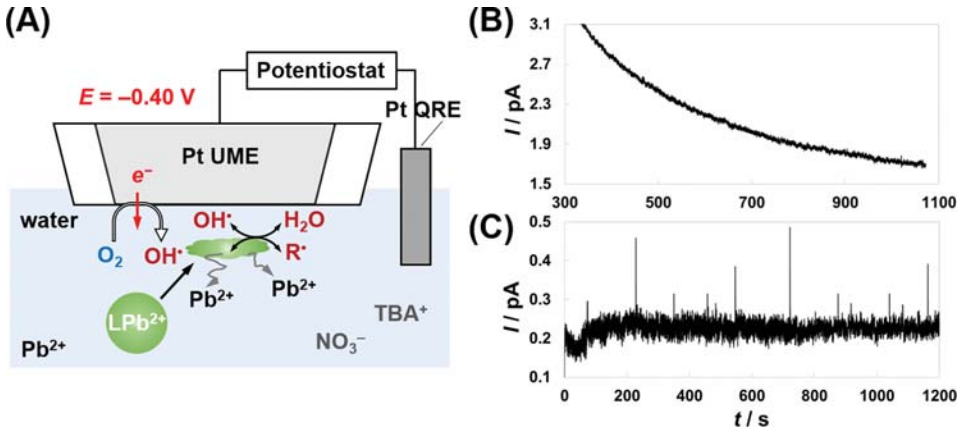

Figure 3. (A) Schematic view of hydroxyl radical ($HO^{\cdot}$) formation under a cathodic potential (E = −0.40 V vs Pt QRE) applied to a Pt UME and the subsequently induced degradation or rupture of NEs causing the leakage of preconcentrated Pb^{2+} from a NE, which leads to a highly diluted concentration of Pb^{2+} in the proximity of a Pt UME and no detectable current signals during SEE measurements. (B) I−t curves during SEE measurements without $HO^{\cdot}$ radical scavengers in the aqueous bulk solution containing 10 μM $Pb(NO_3)_2$ and 8 pM Pb^{2+}-selective NEs. (C) I−t curves during SEE measurements with $HO^{\cdot}$ radical scavengers, 5 mM of $(NH_4)_2SO_3$ in the aqueous bulk solution containing 10 μM $Pb(NO_3)_2$, and 8 pM Pb^{2+}-selective NEs.

radicals such as carbon radicals that could also start chain reactions.[26,28−30]

$$OH^{\cdot} + RH \rightarrow R^{\cdot} + H_2O \quad (2)$$

Previously, Hapiot and co-workers also reported the degradation of an organic layer by $HO^{\cdot}$ radicals electrochemically generated at neutral pH, where tip-generated $HO^{\cdot}$ radicals enabled surface micropatterning on the organic layer-coated substrate by scanning electrochemical microscopy.[26]

Accordingly, we envisage a scenario where $HO^{\cdot}$ radical production by ORR at a Pt UME could induce degradation or damages on NEs near the surface of a Pt UME and finally rupture them, where the surfactants of Pluronic F-127 and DOS are susceptible to the reaction with $HO^{\cdot}$ radicals (Figure 3A). The resultant leakage of Pb^{2+} from a ruptured NE yields a highly diluted concentration of Pb^{2+} in the proximity of a Pt UME, thereby hampering detectable current signals during SEE (Figure 3B). This speculation strongly implies that the appropriate suppression of $HO^{\cdot}$ radical formation at the surface of a Pt UME under a cathodic potential should be needed to protect the intactness of NEs upon their collisions onto a Pt UME and to attain the highly sensitive sensing of Pb^{2+} partitioned to NEs during SEE measurements. Although O_2 in aqueous solution can be removed by N_2 gas purging, gas purging technically interrupts sensitive SEE measurements due to the burst of NEs induced by a direct contact with air bubbles as well as high noise level in current responses.

Sulfite anion (SO_3^{2-}) is a well-known scavenger of $HO^{\bullet}$ radical production owing to its mild oxidizing power.[31,32] The reaction of SO_3^{2-} with $HO^{\cdot}$ radical produces sulfite radical, $SO_3^{\cdot-}$, as below[31]

$$SO_3^{2-} + HO^{\cdot} \rightarrow SO_3^{\cdot-} + OH^- \quad (3)$$

Subsequently, the decay of $SO_3^{\cdot-}$ due to the self-reaction occurs as[31]

$$2SO_3^{\cdot-} \rightarrow S_2O_6^{2-} \text{ or } SO_3 + SO_3^{2-} \quad (4)$$

In addition, $SO_3^{\cdot-}$ can be electrochemically reduced at a Pt UME[32]

$$SO_3^{\cdot-} + e^- \rightarrow SO_3^{2-} \; E = 0.63 \text{ V at pH} > 7 \quad (5)$$

Based on all relevant reactions concomitantly occurring near a Pt UME at a cathodic potential (−0.4 V vs Pt QRE), catalytic $HO^{\cdot}$ radical scavenging by SO_3^{2-} can be considered in SEE for a highly sensitive detection of Pb^{2+} with retaining intact NEs. Due to the catalytic property of SO_3^{2-} scavenging reaction, even a small concentration of SO_3^{2-} (≈1 mM) is sufficient to provide a quantitative formation of $SO_3^{\cdot-}$, where SO_3^{2-} can be steadily replenished by either a decay reaction or electrochemical reduction of $SO_3^{\cdot-}$ under our experimental setup.[32] Thereby, ca. 5 mM of $(NH_4)_2SO_3$ is introduced to suppress the formation of $HO^{\cdot}$ radicals at a Pt UME in SEE.

As shown in Figure 3C, a series of distinctly sharp current spikes are observed upon the collision of NEs onto a Pt UME during SEE measurements in the presence of 5 mM $(NH_4)_2SO_3$ and 2 mM $TBANO_3$ with 10 μM $Pb(NO_3)_2$ in aqueous solution, whereas no current spikes are seen without 5 mM $(NH_4)_2SO_3$ (Figure 3B). This clear contrast in SEE data confirms that the successful suppression of $HO^{\cdot}$ radical formation enables us to maintain the intactness of NEs, preserve Pb^{2+} partitioned/preconcentrated inside a NE, and yield measurable current signals from Pb^{2+} reduction upon the collision of an individual NE onto a Pt UME.

Large Partition Coefficient of Pb^{2+}−Pb Ionophore IV at an Intact NE Corroborated by Molecular Dynamics Simulation. To attain an ultralow detection of Pb^{2+} in blood using Pb^{2+}-selective NI-SEE, the effective separation of Pb^{2+} from the sample to a NE and the significant preconcentration via extraction are required. Particularly, the efficient extraction of Pb^{2+} relies on the large partition coefficient of Pb^{2+}−Pb ionophore IV at an intact NE as a key component for the highly sensitive detection of Pb^{2+}. Previously, we revealed that the extremely large partition coefficient of aromatic compounds inside an intact NE is attributed to the intermolecular interactions via noncovalent bonding, i.e., H-bonding and n−π* between a NE inner component, DOS, and aromatic compound.[20] For example, the partition coefficient of 2-aminobiphenyl (2-ABP) in an intact NE filled with DOS is enhanced up to 10 orders of magnitude compared to the bulk phase determined by SEE measurements as well as molecular dynamics (MD) simulations.[20]

https://doi.org/10.1021/acs.langmuir.3c03138
Langmuir 2024, 40, 3004−3014

Hereby, the intermolecular interaction between Pb^{2+}−Pb ionophore IV and DOS inside the NE was studied by MD simulations. A stabilized conformer of 1 Pb^{2+}, 1 Pb ionophore IV, and 1 DOS exhibits a complex of Pb^{2+} ion and Pb ionophore IV with 1:1 stoichiometry embraced by DOS, where two oxygens in the ester group of DOS and the adjacent two aromatic rings in calixarene of lead ionophore IV locate within 3.3−3.9 Å, thus interacting via noncovalent bonding of $n-\pi^*$ between DOS and the aromatic ring (green solid lines in Figure 4A or green/pink solid lines in Figure 4B). The

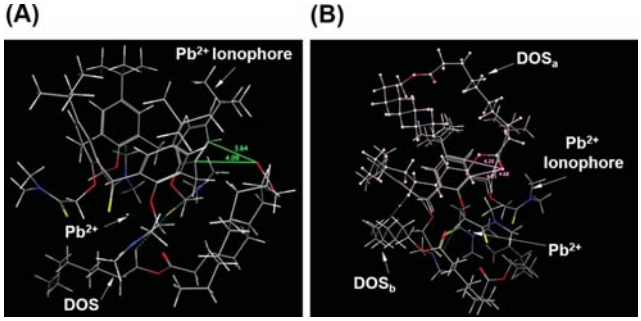

Figure 4. Geometry-optimized structures of (A) 1 Pb^{2+}, 1 Pb−ionophore IV, and 1 DOS and (B) 1 Pb^{2+}, 1 Pb−ionophore IV, and 2 DOS. The interactions between the lone pair (O in DOS) and the π system of aromatic rings (Pb−ionophore IV) are depicted with green and pink solid lines. Hydrogen bondings are represented with green and blue dotted lines.

significance of the lone pair−π interaction (or referred to as $n-\pi^*$) has been noted as attractive and moderately strong, with the energy level up to −94.5 kJ/mol.[33,34] In the condensed phase like a NE, van der Waals interaction accounts for additional stabilization within the adsorption domain compared to the bulk phase as well.[35,36] Moreover, H bonding is formed between the hydrogen of the alkyl group in DOS and the aromatic ring of Pb^{2+} ionophore IV as the H-bond acceptor[37] (green dotted line in Figure 4A). Considering the collective behavior at various ratios between Pb ionophore IV and DOS molecules inside a NE, the resulting conformers of Pb^{2+}, Pb ionophore IV, and DOS exhibited large stabilization with $\Delta G^\circ < -0.3$ GJ/mol throughout various intermolecular interactions (Figure 4). Resultantly, multiple forms of intermolecular interactions could stabilize Pb^{2+}−Pb ionophore IV inside a NE, thereby contributing to the large partition coefficient of Pb^{2+}−Pb ionophore IV at an intact NE.

Notably, the large formal complex formation constant, log β_n, for Pb ionophore IV and Pb^{2+} with a strong 1:1 complex was reported as 15.2−15.9, determined in the DOS organic membrane phase by potentiometric methods.[23] This β_n being higher by 6 orders of magnitude than that of K^+ with valinomycin represents not only the high stability of the complex[23] but also a high selectivity with nearly no major interfering ions.[24] The inherently large formation constant for Pb ionophore IV and Pb^{2+} along with the additional intermolecular interactions of Pb ionophore IV inside a NE leads to the effective extraction of Pb^{2+} from the aqueous sample solution into a Pb^{2+}-selective NE, which enables to sufficiently preconcentrate Pb^{2+} into a NE and amplify the electrochemical signals, i.e., cathodic currents of Pb^{2+} for the highly sensitive measurements in SEE.

It should be noted that the extracted amount of Pb^{2+} in NEs is governed by not only the partition coefficient of Pb ionophore IV and β_n but also the amount of a cation exchanger, KTFPB, inside a NE as the limiting reagent in the present system. Due to the complexity under multiple governing factors, the partition coefficient of Pb ionophore IV cannot be accurately determined as before. We, however, approximately estimated the partition coefficient of Pb ionophore IV at an intact NE as ca. 9 orders of magnitude under the condition of Pb^{2+} as a sole limiting factor among a series of SEE experiments (see SI and Figure S11). Markedly, this large partition coefficient of Pb ionophore IV at a NE is consistent with the predicted MD simulation results and close to one for 2-ABP at an intact NE studied before.[20]

Ultrasensitive Pb^{2+} Detection with Pb^{2+}-Selective NE-Integrated Single-Entity Electrochemistry. As schematically illustrated in Figure 1B, SEE was performed, where a Pt UME applied with a constant potential at −0.4 V versus Pt QRE was immersed in the aqueous solution containing Pb^{2+} at concentrations lower than 10 μM, $HO^{\cdot}$ radical scavenger (5 mM $(NH_4)_2SO_3$), supporting electrolytes (2 mM $TBANO_3$), and freshly prepared NEs embedded with Pb^{2+} ionophore IV. This aqueous solution was vortexed for 15 min right after adding NEs to ensure that the system was under equilibrium as well as homogeneous mixing. In order to realize real-time measurements, the efficient and rapid extraction of Pb^{2+} into Pb^{2+}-selective NEs is crucial. In this case, a short loading time is anticipated from the high diffusional flux of Pb^{2+} to a NE owing to the efficient three-dimensional mass transfer of Pb^{2+} to the small dimension of NEs. For example, a diffusional flux of Pb^{2+} to the surface of a NE under a steady state is written below[38]

$$J = \frac{D_{Pb^{2+}} \cdot C_{Pb^{2+}inaq}}{r_{NE}} \tag{6}$$

where $D_{Pb^{2+}}$ and $C_{Pb^{2+}inaq}$ are the diffusion coefficient and concentration of Pb^{2+} in the aqueous solution, respectively, and r_{NE} is the radius of a NE. From this flux, with the assumption of the instantaneous partitioning and extraction of Pb^{2+} at the interface between NE and solution, the diffusion-limited loading time for aqueous Pb^{2+} to a NE, τ, can be estimated by[38]

$$\tau = \frac{r_{NE}^2 \cdot C_{L\ in\ NE}}{3D_{Pb^{2+}} \cdot C_{Pb^{2+}inaq}} \tag{7}$$

where $C_{L\ in\ NE}$ is the ionophore concentration in a NE or a filling capacity of a NE for Pb^{2+} extracted from aqueous solution. The amount of Pb ionophore IV inside a NE is concentrated to 2.20 M with a cation exchanger, KTFPB, at 1.73 M, considering ∼2600-fold of the preconcentration factor.[22] As divalent Pb^{2+} exchanges with two of K^+ during extraction into a NE, the maximum filling capacity ($C_{max\ filling}$) of each NE for Pb^{2+} would be 0.86_5 M, considering the cation exchanger, KTFPB, as a limiting reagent. With $D_{Pb^{2+}} = 9.39 \times 10^{-6}$ cm^2/s[23] and 20 nm radius of a NE, 0.25 μM−2.5 nM range of Pb^{2+} in aqueous solution in the presence of 8 pM−80 fM NEs can be accumulated into each NE to yield 0.865 M Pb^{2+} in a NE in 480 ms−48 s, respectively, where the formation of 1:1 Pb−ionophore complex is considered.[23,24] The expected loading times would be rapid enough to perform real-time SEE measurements under true equilibrium, thereby enabling in situ separation, preconcentration, and detection of Pb^{2+} from the aqueous sample.

https://doi.org/10.1021/acs.langmuir.3c03138
Langmuir 2024, 40, 3004−3014

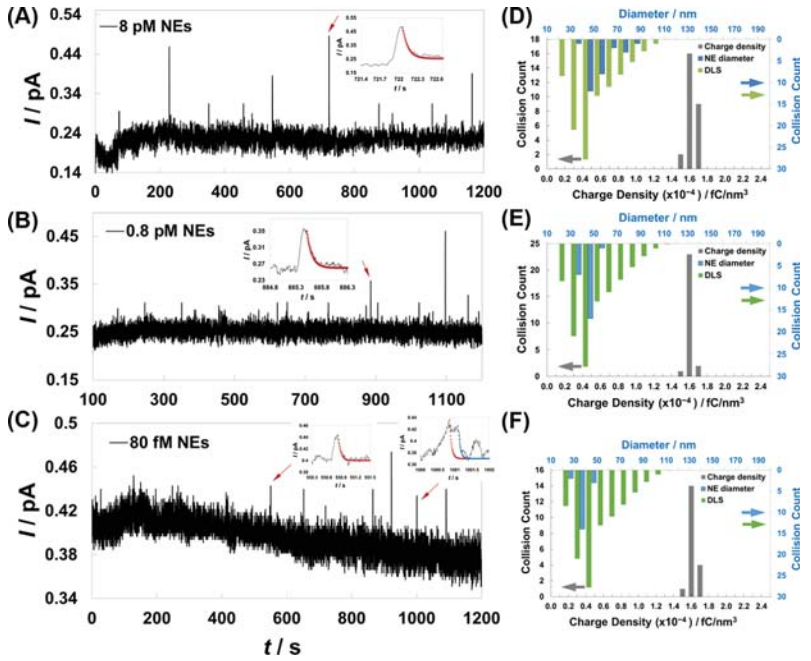

Figure 5. $I-t$ curves during SEE measurements in the presence of (A) 10 μM $Pb(NO_3)_2$ and 8 pM Pb^{2+}-selective NEs, (B) 0.1 μM $Pb(NO_3)_2$ and 0.8 pM Pb^{2+}-selective NEs, and (C) 10 nM $Pb(NO_3)_2$ and 80 fM Pb^{2+}-selective NEs. All of the aqueous bulk solutions contain 5 mM $(NH_4)_2SO_3$ and 2 mM $TBANO_3$ as hydroxyl radical scavengers and supporting electrolytes, respectively. Each inset exhibits magnified current spikes fitted with the bulk electrolysis model (red and blue open circles). (D–F) Distribution curves of charge density at each single NE (gray bars) and NE sizes determined by both DLS (green bars) and SEE measurements (blue bars), corresponding to (A–C), respectively.

In Figure 5, three sets of SEE data measured at different NE concentrations such as 8.0 pM, 0.8 pM, and 80 fM are depicted. In each respective concentration of NEs, we conducted SEE by varying the Pb^{2+} concentration in aqueous solution by 3 orders of magnitude. The first set of SEE was performed with 8.0 pM NEs in the presence of 10 μM Pb^{2+} in an aqueous solution. $i-t$ curve was obtained with a series of current spikes showing nearly similar current magnitudes (Figure 5A). Each current spike showed an exponential decay with time, indicating a bulk electrolysis behavior inside a NE. In the Figure 5A inset, a good agreement between the experimental $i-t$ (black solid line) and the theoretical one (red open circles) evidently represents that the extracted Pb^{2+} resides inside a NE and undergoes an electrochemical reduction at a contact point between the NE and Pt UME (see SI). By integrating each current spike, charges required to reduce Pb^{2+} partitioned in each NE were collected, where current spikes at least 3x larger than the background noise signal were counted.

From the integrated charges (Q), diameters (d_{NE}) of NEs and the resulting charge densities (Q/V) could be estimated as[19]

$$d_{NE} = 2\sqrt[3]{\frac{3Q}{4\pi\cdot 2\cdot FC_{\text{Filling in NE}}}} \tag{8}$$

where d_{NE} (nm) is a diameter of NEs, Q (C) is a charge integrated from a current spike in $i-t$ curves, F is the Faraday constant (96,485 C/mol), and $C_{\text{filling in NE}}$ (M) is the concentration of Pb^{2+} filling a NE. Considering a uniform filling of NEs with Pb^{2+} under equilibrium, $C_{\text{filling in NE}}$ is determined by[19]

$$C_{\text{filling in NE}} \approx \left[\frac{V_{\text{total}}}{V_{\text{NE}}}\right]\cdot C^{\text{tot}}_{Pb^{2+}} < C_{\text{max filling}}, \text{ then } C_{\text{filling in NE}} \tag{9}$$

$$C_{\text{filling in NE}} \approx \left[\frac{V_{\text{total}}}{V_{\text{NE}}}\right]\cdot C^{\text{tot}}_{Pb^{2+}} \geq C_{\text{maxfilling}}, \text{ then } C_{\text{maxfilling}} \tag{10}$$

where V_{NE} and V_{total} are the volumes of the NE phase and the sum of aqueous and NE phases, respectively, $C_{\text{filling in NE}}$ is the concentration of Pb^{2+} extracted to a NE, and $C_{\text{max filling}}$ is the maximum filling capacity of a NE, i.e., the max concentration of Pb^{2+} filling a NE. In the case of 8.0 pM NEs with 10 μM Pb^{2+} in aqueous solution, $C_{\text{filling in NE}} = C_{\text{max filling}} = 0.86_5$ M.

The discrete size distribution of NEs determined from each current spike in Figure 5A is illustrated in Figure 5D (blue bars). The resultant d_{NE} ranges 30–80 nm with a peak at 40 nm, which agrees well with the size distribution characterized by dynamic light scattering (DLS) (green bars). This good agreement validates $C_{\text{filling in NE}}$ with the assumption of uniformly filled NEs under equilibrium. The corresponding charge density (Q/V) at each NE is subsequently estimated, and its distribution is plotted in Figure 5D (gray bars). A narrow distribution of charge densities with the highest probability at 1.65 ($\pm$0.1) $\times$ 10^{-4} fC/nm^3 is obtained for this given condition. A series of SEEs were conducted in the presence of 8.0 pM NEs with varying Pb^{2+} concentrations from 10 μM to 10 nM, and each current spike was analyzed to estimate the size distribution of NEs and the corresponding charge densities as well (see SI and Figure S5).

Also, we systematically varied the NE concentration in SEE. In the second set of SEE in Figure 5B, under 0.8 pM NEs and 100 nM Pb^{2+} in aqueous solution, the $i-t$ curve exhibits a series of current spikes, which individually feature bulk

https://doi.org/10.1021/acs.langmuir.3c03138
Langmuir 2024, 40, 3004–3014

electrolysis behavior (inset in Figure 5B). Integrated charges (Q) from discrete current spikes, the estimated d_{NE} using eqs 8−10, and the subsequent charge densities at each NE are analyzed in the same manner as above and plotted together. A good consistency between the electrochemically determined d_{NE} (blue bars) and DLS data (green bars) could be obtained, thereby validating $C_{filling\ in\ NE}$ in the given condition as well (in the case of 0.8 pM NEs with 100 nM Pb^{2+} in aqueous solution, $C_{filling\ in\ NE} = C_{max\ filling} = 0.865$ M). The resultant charge densities at each NE for Pb^{2+} reduction are narrowly distributed with a peak at 1.6_5 (± 0.1) $\times 10^{-4}$ fC/nm^3 (gray bars in Figure 5E). Continuously, another series of SEE were performed in the presence of 0.8 pM NEs with varying Pb^{2+} concentrations from 100 to 1.0 nM, where each current spike was analyzed to estimate the size distribution of NEs and the corresponding charge densities as well (see SI and Figure S6).

In the last set of SEE in Figure 5C, the NE concentration was further decreased to 80 fM, where 10 nM Pb^{2+} in aqueous solution was studied by SEE. A series of current spikes appeared in the resulting $i-t$ curve, consistently showing bulk electrolysis behavior (insets in Figure 5C). As analyzed above, Q from individual current spikes was separately integrated, and each corresponding d_{NE} was calculated based on eqs 8−10 and compared with DLS data (blue and green bars, respectively in Figure 5F). The electrochemically determined d_{NE} matches well with the DLS data, indicating the validity of $C_{filling\ in\ NE}$ (in the case of 80 fM NEs with 10 nM Pb^{2+} in aqueous solution, $C_{filling\ in\ NE} = C_{max\ filling} = 0.86_5$ M). Subsequently, charge densities estimated at each NE result in a compact distribution at the peak of 1.6_5 (± 0.1) $\times 10^{-4}$ fC/nm^3 (gray bars in Figure 5F). More SEE measurements were further followed in the presence of 80 fM NEs with varying Pb^{2+} concentrations from 10 to 0.1 nM, and each current spike was analyzed to estimate the size distribution of NEs and the corresponding charge densities (see SI and Figure S7).

Notably, the preconcentration factor by introducing NEs reaches up to 6−8 orders of magnitude, which is attributed to the large partition coefficient of Pb^{2+}−Pb ionophore IV at an intact NE as well as the high stability of the Pb^{2+}−Pb^{2+} ionophore complex. This preconcentration factor leads to enhanced current signals in the present SEE measurements, thereby enabling a highly sensitive detection of Pb^{2+} dissolved in the aqueous solution at the trace level.

Quantification in Pb^{2+}-Selective NE-Integrated Single-Entity Electrochemistry. *Calibration Curves with Standard Solutions in SEE Measurements.* We collected charge densities determined at individual NEs in SEE measurements at various concentrations of NEs and Pb^{2+} in the aqueous solutions and constructed calibration curves, where charge densities at single NEs are plotted as a function of total concentration of Pb^{2+}. In Figure 6, three branches of curves correspond to the NE concentrations of 8.0 pM, 0.8 pM, and 80 fM, where sigmoidal trends appear with an exponential dependence and a saturated region. The saturated region appears due to the limited maximum capacity of each NE for filling Pb^{2+}. Except the saturated region, each curve is fitted with the exponential function. The respective exponential equations and R^2 correlation coefficients (≈0.99) are shown in Figure 6. Noticeably, three branches of curves exhibited the same exponential factors with different pre-exponential factors, thereby resulting in almost laterally shifted but nearly identical shaped curves. It implies that the sensitivity of SEE measurements can be modulated by adjusting the NE

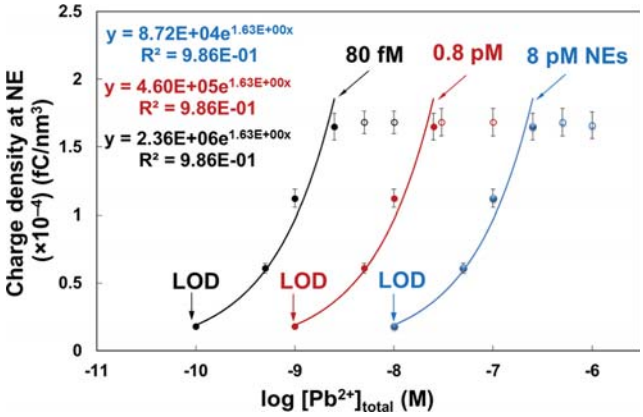

Figure 6. Charge density plots depicting charge densities at single NEs as a function of the logarithm of total Pb^{2+} concentrations in the presence of 8 pM (blue circles), 0.8 pM (red circles), and 80 fM (black circles) Pb^{2+}-selective NEs in aqueous solutions. Each curve exhibits a sigmoidal trend, where LODs are 100 pM, 1 nM, and 10 nM (i.e., 20 ppt, 0.2 ppb, and 2.0 ppb) for 80 fM, 0.8 pM, and 8 pM NEs, respectively. Within the dynamic ranges, calibration curves for the three branches are fitted with the exponential equations having pre-exponential and exponential factors, as shown in the figure legend.

concentrations with respect to the total concentration of Pb^{2+}, thereby enhancing the sensitivity by decreasing the NE concentrations and lowering the LOD for Pb^{2+} up to 100 pM, i.e., 20 ppt in the presence of 80 fM NEs. This charge density plot can be further utilized for the quantitative analysis of Pb^{2+} in unknown samples.

Quantification of Pb^{2+} in Spiked Blood Samples. To confirm the sensing performance of Pb^{2+}-selective NI-SEE and validate the analytical utility of the charge density plot, we studied spiked blood samples. Spiked blood samples were prepared with blood serums stepwisely filtered using two syringe filters with pore diameters of 0.45 and 0.1 μm, respectively, to remove large blood proteins and clots prior to measurements. A serial dilution of 200 nM $Pb(NO_3)_2$ blood serum solution was made to accurately prepare 2.0 nM Pb^{2+}-spiked blood samples. This 2.0 nM is 20 times higher than the LOD, thus being considered as an LOQ level with reasonable accuracy. Subsequently, spiked blood samples were mixed with 8.0 pM, 0.8 pM, and 80 fM of Pb^{2+}-selective NEs separately by 15 min vortex, and SEE was performed with each blood sample. Importantly, we confirmed the negligible biofouling of a Pt UME in the blood serum samples prior to the SEE measurements (see SI and Figure S10).

In Figure 7, each $i-t$ curve was monitored during SEE measurements, where the characteristic current spikes clearly appeared in the presence of 0.8 pM and 80 fM NEs. Also, current decays in each current spike follow the bulk electrolysis model, indicating extraction and preconcentration of Pb^{2+} inside Pb^{2+}-selective NEs (insets in Figure 7B,C). However, any discernible current spike larger than 3 times the background noise level was not observed at 8.0 pM NEs (Figure 7A). This could be due to insufficient sensitivity in SEE measurements beyond the LOD at 8.0 pM NEs. From each set of SEE data at 0.8 pM and 80 fM NEs, charge densities at single NEs were discretely determined from the charges estimated by the integration of individual current spikes and the constant $d_{NE} \approx 41$ nm confirmed by DLS (Figure 7D,E). The resultant charge densities exhibited a nearly narrow distribution with the highest probability at 0.5_9

https://doi.org/10.1021/acs.langmuir.3c03138
Langmuir 2024, 40, 3004−3014

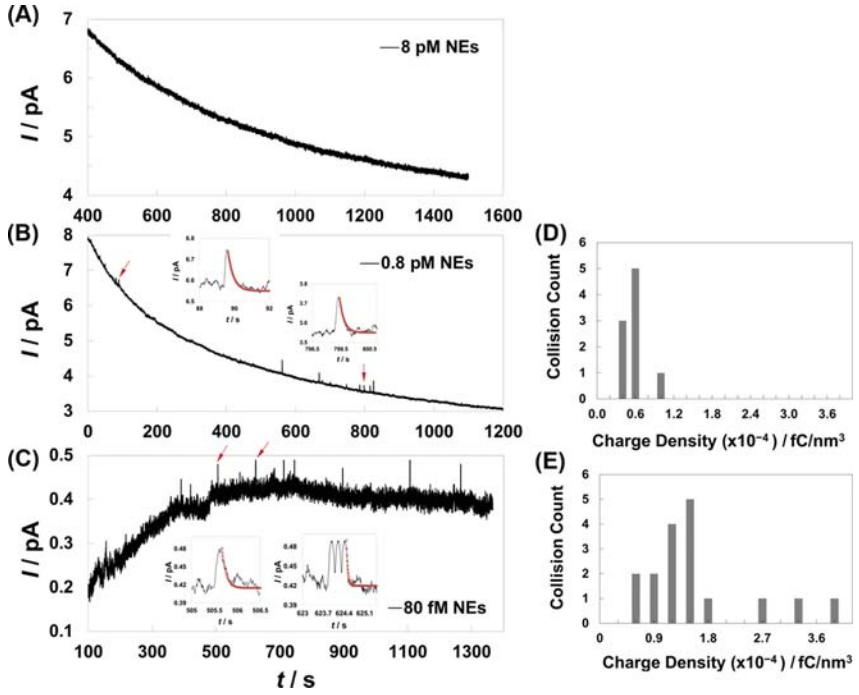

Figure 7. (A–C) I–t curves during SEE measurements with spiked blood samples in the presence of 8.0 pM, 0.8 pM, and 80 fM Pb^{2+}-selective NEs, respectively. Note that no discernible current spikes appeared in (A), whereas a series of characteristic current spikes were observed in (B and C). In each inset, magnified current spikes were fitted with the bulk electrolysis model (red open circles). (D and E) Distribution curves of charge densities at single NEs corresponding to (B and C), respectively, where charge densities were discretely estimated from the integration of individual current spikes in i–t curves, and their distributions were plotted.

($\pm$0.2) $\times$ 10^{-4} and 1.5_8 ($\pm$0.3) $\times$ 10^{-4} fC/nm^3 for 0.8 pM and 80 fM NEs, respectively. To quantify the total Pb^{2+} concentration, a charge density plot was utilized as a calibration curve (Figure 6).

For quantification, we defined the accuracy range as 35–98% of the maximum charge density (1.6_7 $\times$ 10^{-4} fC/nm^3) in the charge density plot (Figure 6), where the slope of the curve is sufficiently steep to sensitively associate the charge densities in NEs with the analyte concentration in total solution. Only the upper limit and lower limit of analyte concentration can be determined in the range of less than 35% and higher than 98% of the maximum charge density, respectively. In fact, current signals that are too small during SEE measurements can cause imprecise integration for estimating charge densities at NEs, thereby affecting both precision and accuracy in the quantification. Also, due to a saturated region in the charge density plot, charge densities at NEs beyond 98% of the maximum value cannot subtly distinguish different analyte concentrations in the total solution, thus limiting the quantification capability in the given analysis. Hereby, both charge densities, 0.5_9 ($\pm$0.2) $\times$ 10^{-4} and 1.5_8 ($\pm$0.3) $\times$ 10^{-4} fC/nm^3 for 0.8 pM and 80 fM NEs, respectively, fall within the defined accuracy range.

Using the calibration curve within the accuracy range, each charge density, 0.5_9 ($\pm$0.2) $\times$ 10^{-4} fC/nm^3 for 0.8 pM NEs and 1.5_8 ($\pm$0.3) $\times$ 10^{-4} fC/nm^3 for 80 fM NEs could determine Pb^{2+} concentrations in total blood samples as 4.97 ($\pm$2.20) nM and 2.00 ($\pm$0.06) nM, respectively. Markedly, 2.00 ($\pm$0.06) nM Pb^{2+} estimated with 80 fM NEs matches well with the true Pb^{2+}concentration (i.e., 2.0 nM) with a reasonable precision in two sets of SEE measurements. However, 4.97 ($\pm$2.20) nM estimated with 0.8 pM NEs was 2.5-fold larger than the true value with a larger uncertainty. Note that the charge density determined at 0.8 pM NEs was positioned marginally in the accuracy range, thereby leading to less accuracy and precision in the quantification results. Overall, the final test of the spiked blood samples successfully validated our quantitative analysis, with Pb^{2+}-selective NI-SEE exhibiting a high accuracy and precision. Moreover, real human blood serums containing a Pb^{2+} spike at 2.0 nM, i.e., 0.4 ppb, could be reliably studied by observing the negligible biofouling or matrix effect, while an unprecedentedly low LOD up to 0.1 nM, i.e., 20 ppt, for Pb^{2+} was achieved in aqueous solutions. Considerably, this sensing performance is superior to spectroscopic methods[9] and general electrochemical approaches and nearly comparable to inductively coupled plasma mass spectrometry (ICP-MS).[10]

Theoretically, if we introduce 8 fM and 80 pM of NEs to this single-entity electrochemistry, we can cover even wider ranges of Pb^{2+} concentration in unknown samples for accurate determination within 10 pM–10 μM. However, at 80 pM NEs, we anticipate the multiple and overlapped current spikes due to c.a. 10-fold increase in the collision frequency than the 8 pM NE case.[22] We definitely want to avoid overlapped current spike responses since they interrupt the accuracy and precision in data analysis when charge densities from each NE are estimated. Likewise, at 8 fM NEs, the technical concern would be very rare current spike responses during single-entity electrochemistry due to too low collisional frequency.[22] Overall, we strategically optimize the NE concentration ranges in this proof-of-concept work, which can successfully target the ultratrace level analysis at tens of parts per trillion–subparts per million level of lead in unknown samples.

For the real-world applications of this demonstrated sensing system, we, however need to consider the potential hampering factor in the accurate determination of blood lead, such as the

https://doi.org/10.1021/acs.langmuir.3c03138
Langmuir 2024, 40, 3004–3014

strong complexation between glutathione (GSH) and Pb^{2+} via coordination with the cysteine thiolate group in blood.[39] Unlike uncomplexed Pb^{2+}, the complexed Pb^{2+} with GSH cannot be properly extracted to a nanoemulsion, thereby causing an underestimation of the blood lead level in NI-SEE. In this case, the pretreatment of blood with GSH peroxidase could be a possible approach to minimize errors in blood lead determination. GSH peroxidase will oxidize GSH to oxidized glutathione dimer with a disulfide bond, i.e., GSSG,[40] which does not complex with Pb^{2+}.[41] Accordingly, complexed Pb^{2+} can be released from GSSG, and the consequent Pb^{2+}, i.e., uncomplexed Pb^{2+}, undergoes extraction to Pb^{2+} ion-selective NEs for sensitive and accurate sensing in NI-SEE measurements. Another consideration would be potential interference from Ag^+ and Hg^{2+} in our Pb^{2+} ion-selective NE system. Although the high selectivity of Pb ionophore IV has been reported for most of the cations,[24] the low selectivity of thioamide bonds to Ag^+ ($\log K_{Pb,Ag} = 1.5$) or Hg^{2+} ($\log K_{Pb,Hg} = 0.6$) has been an emerging concern as well.[42−44] For the anticipated drawback of Pb ionophore selectivity, we can consider additional pretreatment or an electrochemical method to overcome the possible interference. Hg^{2+} precipitates at pH 2.4 or higher;[45] thus, at the physiological pH of the blood sample, most of Hg^{2+} can be separated and filtered out by forming a precipitate as a form of $Hg(OH)_2$. Furthermore, Ag^+ binding with Pb ionophore IV can be differentiated from Pb^{2+} by electrochemical reduction at a more positive potential ($E^0_{Ag} = 0.7999$ V vs NHE)[38] than Pb^{2+} reduction ($E^0_{Pb} = -0.1251$ V vs NHE),[38] where nanoemulsion-integrated single-entity electrochemistry can be performed at a positive potential, e.g., $E_{red} = 0.2$ V versus QRE to screen Ag^+ sensing in the given samples.

The significance of this work resides in the direct applicability to real blood samples with an ultralow LOQ up to sub-ppb level, thereby being utilized for biomedical analysis such as monitoring elevated blood lead (EBL) relevant to children's brain health. Considering the neurotoxic effect regarding the unestablished threshold of blood lead,[8] we envision that point-of-care blood lead testing with this highly sensitive approach will be broadly explored for biomedical as well as neurotoxicological research. Furthermore, the application of ion-selective NI-SEE with various types of ionophores or chelators can expand to the environmental/biomedical analysis to track the ultratrace level of heavy metal ions or ionic toxicants in various aqueous samples such as water system and biofluids. Fundamentally, the demonstrated approach can interrogate the stoichiometry of target ion−ionophore recognition inside a NE as a nanoreactor.

CONCLUSIONS

We have successfully explored the sensing performance of Pb^{2+}-selective NE-integrated SEE approach toward trace amount of Pb^{2+} in water or blood serums. Markedly, it exhibits a selective detection behavior toward Pb^{2+} via high thermodynamic selectivity based on ion−ionophore recognition and a high sensitivity due to an extremely large partition coefficient of Pb^{2+}−Pb ionophore in NEs via intermolecular interactions, thus enabling a large preconcentration factor up to 6−8 orders of magnitude. The intermolecular interaction between Pb ionophore IV and DOS, a plasticizer of a NE, was validated by MD simulations. A series of SEE measurements enabled us to construct unique calibration curves correlating the charge densities required for the reduction of preconcentrated Pb^{2+} in each NE, with the Pb^{2+} concentration in the total solution, and exhibited a detection limit of 0.1 nM, i.e., 20 ppt for Pb^{2+} in aqueous solution, which is considered superior to some previously reported electrochemical or spectroscopic approaches, and almost equivalent to ICP-MS. 2.0 nM, i.e., 0.4 ppb of Pb^{2+} in human blood serums, could be reliably detected with negligible biofouling or insignificant matrix effect. Given its excellent detection performance as well as its high durability resistant to biofouling, our newly established approach offers great prospects as a sensor for environmental and biomedical applications.

METHODS

Chemicals. Pluronic F-127 (F-127), bis(2-ethylhexyl)-sebacate (DOS, or castor oil, 97.0%), tetrahydrofuran (THF, 99.9%), lead(II) nitrate ($Pb(NO_3)_2$, 99.0%), and *tert*-butylcalix[4]arene-tetrakis(*N*,*N*-dimethylthioacetamide) (a.k.a., lead ionophore IV) were used as obtained from Sigma-Aldrich. Potassium tetrakis[pentafluorophenyl] borate (KTFPB, 95%) was used as purchased from Boulder Scientific. Also, tetrabutylammonium nitrate ($TBANO_3$, 97%), ammonium sulfite monohydrate ($(NH_4)_2SO_3 \cdot H_2O$, 92%), and ferrocenemethanol (97%) were purchased from Sigma-Aldrich and used as obtained. Tetradodecylammonium tetrakis[pentafluorophenyl]borate ($TDDA^+TFPB^-$) was prepared by metathesis, as reported elsewhere.[46] Nanopure water (18.2 MΩ·cm, TOC 2 ppb; Milli-Q Integral 5 system, Millipore) was used to prepare all of the aqueous electrolyte solutions as well as in NE synthesis.

Synthesis of Nanoemulsion. The synthesis of nanoemulsions is reported elsewhere.[22] Briefly, THF cocktail was prepared by dissolving 1.5 mg of KTFPB, 2.7 mg of lead ionophore (IV), and 250.0 mg of F127 in 3.0 mL of THF in a vial (Fisher Scientific, 8 DR) to form a homogeneous solution. Subsequently, 8.8 μL of DOS was added. This final THF cocktail was mixed for 1 h by using a vortex mixer (Fisher Scientific, Pittsburgh, PA) at 3000 rpm. After mixing, a 0.1 mL aliquot from the mixed THF cocktail was forcefully injected into 4.0 mL of nanopure water in the vial (Fisher Scientific, 4 DR) during vortex mixing at 4000 rpm and continuously vortex-mixed for 2 min. This process was immediately repeated for another batch. The total 8 mL of nanopure water containing the THF cocktail was combined and then homogenized (Kinematica AG, Polytron system PT 10-35 GT, Switzerland) for 2 min at 4900 rpm. In this case, 8 mL is the minimum volume used to suppress froth formation during homogenization (with a 4 DR vial). After homogenization, the solution was further purged with N_2 gas to evaporate THF for 1 h under a flow rate of 40 psi. A volume reduction of roughly 2 mL was observed after the evaporation step. This final solution is a NE stock solution having ca. 400 pM of NEs. NEs are characterized by dynamic light scattering (DLS) and transmission electron microscopy (TEM) for size distribution, zeta potential, and monodispersity (see SI and Figures S3 and S4).

Solution Preparation for SEE Measurements. 0.00414 g of $Pb(NO_3)_2$ was dissolved in 25.0 mL of nanopure water to prepare 0.5 mM stock solution. From this $Pb(NO_3)_2$ stock solution, diluted solutions of 0.25, 0.1, 0.025, 0.01, 0.005, and 0.001 μM were prepared. The electrolyte solution was made with 0.0067 g of $(NH_4)_2SO_3 \cdot H_2O$ and 0.0068 g of $TBANO_3$ dissolved in 10 mL of nanopure water with 5 mM:2 mM composition ratio, respectively.

Spiked Blood Sample Preparation. The commercially available human blood serum sample (single donor human serum off the clot, Innovative Research Inc., MI, US) mixed with 5 mM $(NH_4)_2SO_3 \cdot H_2O$ and 2 mM $TBANO_3$ was filtered using 0.45 and 0.1 μm syringe filters (SLHVR33RS and SLVVR33RS, Millex VV Sterile Syringe Filter unit, PVDF, MilliporeSigma), successively. 200 nM $Pb(NO_3)_2$ solution was added as a spike to human blood serum and diluted to the final concentration at 2 nM.

SEE Measurements. SEE was performed in a two-electrode cell by using a bipotentiostat (CHM8022D, CH Instrument, Austin, TX) at ambient temperature (20 °C). Pt UMEs (1−5 μm diameter) was

https://doi.org/10.1021/acs.langmuir.3c03138
Langmuir 2024, 40, 3004−3014

immersed in the aqueous solution containing 5 mM:2 mM composition of $(NH_4)_2SO_3{\cdot}H_2O$ and $TBANO_3$ as the supporting electrolytes. The cathodic potential of −0.4 V versus the Pt quasi-reference electrode (Pt QRE) was applied to a Pt UME, and amperometric $i-t$ curves were monitored with 0.1 ms sampling time, where cathodic currents as a result of Pb^{2+} reduction were recorded over time, either in the absence or presence of NEs containing Pb^{2+} ionophore IV.

Molecular Dynamics Simulations. Quantum chemistry calculations were carried out using the Molecular Operating Environment (MOE) (2020; Chemical Computing Group ULC, 1010 Sherbooke St. West, Suite #910, Montreal, QC, Canada, H3A 2R7, 2021). Lead ion (II), lead ionophore IV, and DOS were built, and the combination of DOS, lead(II), and lead ionophore IV were geometrically equilibrated. The conformer distribution was found for geometrically equilibrated molecular structures using the Molecular Mechanics, Merck Molecular Force Field (MMFF) calculation method. Over numerous complicated conformers, the most stable structures were chosen and stabilized under the semiempirical PM3 method to find the most stable structures with the least energy values. Thermodynamic parameters for these stabilized conformer structures of DOS, lead ionophore IV, lead(II) with (or without) organic solvent molecules, $CHCl_3$, were implemented with the DFT method and all basis sets. Preceding calculations were performed with the Slater type and B3LYP 631G functions applied in the MOE program for both geometry optimization and thermodynamic energy values.

■ ASSOCIATED CONTENT

Supporting Information

The Supporting Information is available free of charge at https://pubs.acs.org/doi/10.1021/acs.langmuir.3c03138.

> Cyclic voltammetry for Pb^{2+} reduction in organic and aqueous solutions, control experiments in SEE, characterization of Pb^{2+}-selective NEs by DLS and TEM, SEE data and distribution curves of charge densities in single NEs, fitting i−t decay with the bulk electrolysis model, MD simulations of Pb^{2+}−Pb ionophore complex with DOS in organic solvent, fouling tests in blood serums, estimation of a partition coefficient of Pb^{2+}−Pb ionophore IV at an intact NE, and selectivity tests in SEE (PDF)

■ AUTHOR INFORMATION

Corresponding Author

Jiyeon Kim − *Department of Chemistry, University of Rhode Island, Kingston, Rhode Island 02881, United States;* orcid.org/0000-0002-7624-6766; Phone: +1 (401) 874-2143; Email: jkim25@uri.edu

Authors

Hiranya Madawala − *Department of Chemistry, University of Rhode Island, Kingston, Rhode Island 02881, United States*

Surendra Raj Puri − *Department of Chemistry, University of Rhode Island, Kingston, Rhode Island 02881, United States*

Delaney Weaver − *Department of Chemistry, University of Rhode Island, Kingston, Rhode Island 02881, United States*

Complete contact information is available at: https://pubs.acs.org/10.1021/acs.langmuir.3c03138

Notes

The authors declare no competing financial interest.

■ ACKNOWLEDGMENTS

This work was supported by the NSF Career (CHE-2046363), Medical Research Fund (20174373) from Rhode Island Foundation, the Rhode Island Institutional Development Award (IDeA) NIGMS/RI-INBRE early career development award (P20GM103430).

■ REFERENCES

(1) Marthers, C.; Stevens, G.; Mascarenhas, M. *Global health risks: Mortality and burden of disease attributable to selected major risks*; World Health Organization: Geneva, 2009, ISBN: 9789241563871 Global health risks: mortality and burden of disease attributable to selected major risks (who.int).

(2) Sanders, T.; Liu, Y.; Buchner, V.; Tchounwou, P. B. Neurotoxic Effects and Biomarkers of Lead Exposure: A Review. *Rev. Environ. Health* **2009**, *24*, 15−45.

(3) Toxicological Profile for Lead, U.S. Department of Health and Human Services, Public Health Service *Agency for Toxic Substances and Disease Registry*, August 2020. ATSDR Lead Tox Profile (cdc.gov).

(4) *Exposure to lead: A major public health concern*; World Health Organization: Geneva, 2010, Exposure to lead: a major public health concern, 2nd ed. (who.int).

(5) Liu, J.; Liu, X.; Wang, W.; McCauley, L.; Pinto-Martin, J.; Wang, Y.; Li, L.; Yan, C.; Rogan, W. J. Blood Lead Levels and Children's Behavioral and Emotional Problems: A Cohort Study. *JAMA Pediatr.* **2014**, *168*, 737−745.

(6) *Centers for Disease Control and Prevention (CDC), Advisory Committee on Childhood Lead Poisoning Prevention. Low Level Lead Exposure Harms Children: A Renewed Call for Primary Prevention*; CDC: Atlanta, GA; 2012. Low Level Lead Exposure Harms Children: A Renewed Call for Primary Prevention (cdc.gov).

(7) Centers for Disease Control and Prevention (CDC). *Response to Advisory Committee on Childhood Lead Poisoning Prevention Recommendations in "Low Level Lead Exposure Harms Children: A Renewed Call of Primary Prevention*; CDC: Atlanta, GA, 2012. CDC response to Advisory Committee on Childhood Lead Poisoning Prevention recommendations in "Low Level Lead Exposure Harms Children: A Renewed Call of Primary Prevention".

(8) Gilbert, S. G.; Weiss, B. A rationale for lowering the blood lead action level from 10 to 2 microg/dL. *Neurotoxicology* **2006**, *27*, 693.

(9) Parsons, P. J.; Slavin, W. A rapid Zeeman graphite furnace atomic absorption spectrometric method for the determination of lead in blood. *Spectrochimica Acta Part B-Atomic Spectroscopy* **1993**, *48*, 925.

(10) Palmer, C. D.; Lewis, M. E., Jr.; Geraghty, C. M.; Barbosa, F., Jr.; Parsons, P. J. Determination of Lead, Cadmium and Mercury in Blood for Assessment of Environmental Exposure: A Comparison between Inductively Coupled Plasma-Mass Spectrometry and Atomic Absorption Spectrometry. *Spectrochimica Acta Part B-Atomic Spectroscopy* **2006**, *61*, 980−990.

(11) Flanagan, R. J.et al.*Fundamentals of analytical toxicology*; John Wiley & Sons Ltd., 2007.

(12) Haefliger, P.; Jardan, E.; Tempowski, J. *Brief Guide to Analytical Methods for Measuring Lead in Blood*, 2nd ed.; World Health Organization, 2020. ISBN 978-92-4-000977-6, Brief guide to analytical methods for measuring lead in blood, 2nd ed. (who.int).

(13) Wengrovitz, A. M.; Brown, M. J. Advisory Committee on Childhood Lead Poisoning, Division of Environmental and Emergency Health Services, National Center for Environmental Health, Centers for Disease Control and Prevention. Recommendations for blood lead screening of Medicaid-eligible children aged 1−5 years: an updated approach to targeting a group at high risk. *MMWR Recomm. Rep.* **2009**, *58*, 1−11.

(14) Bühlmann, P.; Chen, L. D. *Supramolecular Chemistry: From Molecules to Nanomaterials*; John Wiley & Sons, 2012.

(15) Bakker, E.; Pretsch, E. Modern Potentiometry. *Angew. Chem., Int. Ed.* **2007**, *46*, 5660−5668.

(16) Sokalski, T.; Ceresa, A.; Zwickl, T.; Pretsch, E. Large Improvement of the Lower Detection Limit of Ion-Selective Polymer Membrane Electrodes. *J. Am. Chem. Soc.* **1997**, *119*, 11347−11348.

(17) Ceresa, A.; Bakker, E.; Hattendorf, B.; Günther, D.; Pretsch, E. Potentiometric Polymeric Membrane Electrodes for Measurement of Environmental Samples at Trace Levels: New Requirements for Selectivities and Measuring Protocols, and Comparison with ICPMS. *Anal. Chem.* **2001**, *73*, 343−351.
(18) Szigeti, Z.; Vigassy, T.; Bakker, E.; Pretsch, E. Approaches to Improving the Lower Detection Limit of Polymeric Membrane Ion-Selective Electrodes. *Electroanalysis* **2006**, *18*, 1254.
(19) Sabaragamuwe, S. G.; Madawala, H.; Puri, S. R.; Kim, J. Towards ultralow detection limits of aromatic toxicants in water using pluronic nanoemulsions and single-entity electrochemistry. *Anal. Chim. Acta* **2020**, *1139*, 129−137.
(20) Madawala, H.; Sabaragamuwe, S. G.; Elangovan, S.; Kim, J. In Situ Measuring Partition Coefficient at Intact Nanoemulsions: A New Application of Single-Entity Electrochemistry. *Anal. Chem.* **2021**, *93*, 1154−1160.
(21) (a) Baker, L. A. Perspective and Prospectus on Single-Entity Electrochemistry. *J. Am. Chem. Soc.* **2018**, *140*, 5153−5160. (b) Li, H.; Zhang, X.; Sun, Z.; Ma, W. Rapid Screening of Bimetallic Electrocatalysts Using Single Nanoparticle Collision Electrochemistry. *J. Am. Chem. Soc.* **2022**, *144*, 16480−16489. (c) Sun, Z.; Gu, Z.; Ma, W. Confined Electrochemical Behavior of Single Platinum Nanoparticles Revealing Ultrahigh Density of Gas Molecules inside a Nanobubble. *Anal. Chem.* **2023**, *95*, 3613−3620.
(22) Sabaragamuwe, S. G.; Conti, D.; Puri, S. R.; Andreu, I.; Kim, J. Single-entity electrochemistry of nanoemulsion: The nanostructural effect on its electrochemical behavior. *Anal. Chem.* **2019**, *91*, 9599−9607.
(23) Ceresa, A.; Pretsch, E. Determination of formal complex formation constants of various Pb2+ ionophores in the sensor membrane phase. *Anal. Chim. Acta* **1999**, *395*, 41−52.
(24) Guziński, M.; Lisak, G.; Kupis, J.; Jasiński, A.; Brocheńska, M. Lead (II)-Selective Ionophores for Ion-Selective Electrodes: a Review. *Anal. Chim. Acta* **2013**, *791*, 1−12.
(25) Puri, S. R.; Kim, J. Kinetics of antimicrobial drug ion transfer at a water/oil interface studied by nanopipet voltammetry. *Anal. Chem.* **2019**, *91*, 1873−1879.
(26) Noël, J.-M.; Latus, A.; Lagrost, C.; Volanschi, E.; Hapiot, P. Evidence for OH radical Production during Electrocatalysis of Oxygen Reduction on Pt Surfaces: Consequences and Application. *J. Am. Chem. Soc.* **2012**, *134*, 2835−2841.
(27) Nordberg, J.; Arener, E. S. J. *Free Radical Biol. Med.* **2001**, *31*, 1287.
(28) Anbar, M.; Meyerstein, D.; Neta, P. The Reactivity of Aromatic Compounds toward Hydroxyl Radicals. *J. Phys. Chem.* **1966**, *70*, 2660−2662.
(29) Neta, P.; Dorfman, L. M. Pulse Radiolysis Studies. XIII. Rate Constants for the Reaction of Hydroxyl Radicals with Aromatic Compounds in Aqueous Solutions. *Adv. Chem. Ser.* **1968**, *81*, 222−230.
(30) Jovanovic, S. V.; Jankovic, I.; Josimovic, L. Electron-transfer reactions of alkylperoxy radicals. *J. Am. Chem. Soc.* **1992**, *114*, 9018−9021.
(31) Neta, P.; Huie, R. E. Free-Radical Chemistry of Sulfite. *Environ. Health Perspect.* **1985**, *64*, 209−217.
(32) Erben-Russ, M.; Michael, C.; Bors, W.; Sara, M. Determination of Sufite Radical (SO3•−) Reaction Rate Constants By Means of Competition Kinetics. *Radiat. Environ. Biophys.* **1987**, *26*, 289−294.
(33) Neel, A. J.; Hilton, M. J.; Sigman, M. S.; Tosste, F. D. Exploiting Non-Covalent π Interactions for Catalyst Design. *Nature* **2017**, *543*, 637−646.
(34) Frontera, A.; Bauzá, A. Concurrent Aerogen Bonding and Lone Pair/Anion−π Interactions in the Stability of Organoxenon Derivatives: a Combined CSD and ab initio Study. *Phys. Chem. Chem. Phys.* **2017**, *19*, 30063−30068.
(35) Willemsen, J. A. R.; Myneni, S. C. B.; Bourg, I. C. Molecular Dynamics Simulations of the Adsorption of Phthalate Esters on Smectite Clay Surfaces. *J. Phys. Chem. C* **2019**, *123*, 13624−13636.
(36) Otero-Pazos, P.; Pereira de Abreu, D.; Sendon, R.; Bernaldo de Quiros, A. R.; Angulo, I.; Cruz, J. M.; Paseiro-Losada, P. Determination of Partition Coefficients of Selected Model Migrants between Polyethylene and Polypropylene and Nanocomposite Polypropylene. *J. Chem.* **2016**, *2016*, No. 3952631.
(37) Levitt, M.; Perutz, M. F. Aromatic rings act as hydrogen bond acceptors. *J. Mol. Biol.* **1988**, *201*, 751−754.
(38) Bard, A.J.; Faulkner, L. R.; *Electrochemical Methods: Fundamental and Applications*, 2nd ed.; John Wiley & Sons INC., 2004.
(39) Mah, V.; Jalilehvand, F. Lead (II) Complex Formation with Glutathione. *Inorg. Chem.* **2021**, *51*, 6285−6298.
(40) Xiong, Y.; Uys, J. D.; Tew, K. D.; Townsend, D. M. S-Glutathionylation: From Molecular Mechanisms to Health Outcomes. *Antioxidants & Redox Signaling* **2011**, *15*, 233−270.
(41) Jacquart, A.; Brayner, R.; El Hage Chahine, J.-M.; Ha-Duong, N.-T. Cd^{2+} and Pb^{2+} complexation by glutathione and the phytochelatins. *Chemico-Biological Interactions* **2017**, *267*, 2−10.
(42) Malinowska, E.; Brzózka, Z.; Kasiura, K.; Egberink, R. J. M.; Reinhoudt, D. N. Lead selective electrodes based on thioamide functionalized calix [4] renes as ionophores. *Anal. Chim. Acta* **1994**, *298*, 253−258.
(43) Mehta, P. K.; Jeon, J.; Ryu, K.; Park, S.-H.; Lee, K.-H. Ratiometric fluorescent detection of lead ions in aquatic environment and living cells using a fluorescent peptide-base probe. *J. Hazard, Mater.* **2022**, *427*, No. 128161.
(44) Mehta, P. K.; Lee, J. Y.; Oh, E.-T.; Park, H. J.; Lee, K.-H. Ratiometric Fluorescence Sensing System for Lead Ions Based on Self-Assembly of Bioprobes Triggered by Specific Pb2+-Peptide Interactions. *ACS Appl. Mater. Interfaces* **2023**, *15*, 14131−14145.
(45) Ugrina, M.; Ceru, T.; Nuić, I.; Trgo, M. Comparative Study of Mercury (II) Removal from Aqueous Solutions onto Natural and Iron-Modified Clinoptilolite Rich Zeolite. *Rocesses* **2020**, *8*, 1523.
(46) Kim, J.; Izadyar, A.; Shen, M.; Ishimatsu, R.; Amemiya, S. Ion Permeability of the Nuclear Pore Complex and Ion-Induced Macromolecular Permeation as Studied by Scanning Electrochemical and Fluorescence Microscopy. *Anal. Chem.* **2014**, *86*, 2090−2098.

https://doi.org/10.1021/acs.langmuir.3c03138
Langmuir 2024, 40, 3004−3014